Check for updates

ADVANCED FUNCTIONAL MATERIALS
www.afm-journal.de

Aqueous Room-Temperature Synthesis of Transition Metal Dichalcogenide Nanoparticles: A Sustainable Route to Efficient Hydrogen Evolution

Jing Li, Roger Miró, Angelika Wrzesińska-Lashkova, Jing Yu, Jordi Arbiol, Yana Vaynzof, Alexey Shavel, and Vladimir Lesnyak**

Transition metal dichalcogenides (TMDs) have emerged as a focal point in electrocatalysis, particularly for the hydrogen evolution reaction (HER), owing to their notable catalytic activity, chemical stability, and cost-efficiency. Despite these advantages, the challenge of devising a practical and economical method for their large-scale application in HER remains an unresolved and critical issue. In this study, a facile, scalable, and cost-effective approach is introduced for producing high-yield, catalytically active TMD nanoparticles, including MoS_2, $MoSe_2$, RuS_2, and $RuSe_2$. These nanoparticles are synthesized through an aqueous room-temperature process, which is not only environmentally friendly but also economically feasible for large-scale production. Remarkably, these TMD nanoparticles exhibit versatile catalytic activity across a broad pH range for HER. Among them, $RuSe_2$ nanoparticles demonstrate catalytic performance comparable to that of a commercial Pt/C electrode. Upon scaling up, the nanomaterials show great potential for integration into practical proton exchange membrane water electrolyzers, maintaining high efficiency even at large current densities and exhibiting very stable performance for up to 100 h. This research paves the way to a sustainable synthesis method of high-performance catalysts, tailored for industrial hydrogen production applications.

1. Introduction

Hydrogen, known for its high energy density and environmentally friendly characteristics, has gained significant attention as a sustainable alternative to fossil fuels, whose consumption and associated environmental impacts are a growing concern in modern society.[1] Electrochemical water splitting involves two distinct electrocatalytic reactions: the hydrogen evolution reaction (HER) and the oxygen evolution reaction.[2,3] HER is considered to be an efficient and clean method for hydrogen production, using renewable energy sources.[4,5] At the forefront of this technology is the HER, where platinum (Pt) currently stands as the most efficient electrocatalyst due to its minimal Gibbs free energy for the adsorption of reaction intermediates.[6,7] However, the high cost of Pt is a major obstacle to its widespread application. This challenge has spurred the exploration of nonprecious metal catalysts

J. Li, V. Lesnyak
Physical Chemistry
TU Dresden
Zellescher Weg 19, 01069 Dresden, Germany
E-mail: vladimir.lesnyak@tu-dresden.de

R. Miró, A. Shavel
Eurecat
Centre Tecnològic de Catalunya
Unitat de Tecnologia Química
Marcel·lí Domingo 2, Tarragona 43007, Spain
E-mail: alexey.shavel@eurecat.org

The ORCID identification number(s) for the author(s) of this article can be found under https://doi.org/10.1002/adfm.202404565

© 2024 The Author(s). Advanced Functional Materials published by Wiley-VCH GmbH. This is an open access article under the terms of the Creative Commons Attribution License, which permits use, distribution and reproduction in any medium, provided the original work is properly cited.

DOI: 10.1002/adfm.202404565

A. Wrzesińska-Lashkova, Y. Vaynzof
Chair for Emerging Electronic Technologies
TU Dresden
Nöthnitzer Str. 61, 01187 Dresden, Germany

A. Wrzesińska-Lashkova, Y. Vaynzof
Leibniz-Institute for Solid State and Materials Research Dresden
Helmholtzstraße 20, 01069 Dresden, Germany

J. Yu, J. Arbiol
Catalan Institute of Nanoscience and Nanotechnology (ICN2)
CSIC and BIST
Campus UAB, Bellaterra, Barcelona, Catalonia 08193, Spain

J. Arbiol
ICREA
Pg. Lluís Companys 23, Barcelona, Catalonia 08010, Spain

that offer low overpotential and high stability, aiming to replace Pt-based catalysts. In this context, transition metal dichalcogenides (TMDs) have emerged as a promising alternative due to their earth abundance and potentially high activity for electrocatalytic HER.[8,9]

The development of TMD-based catalysts for industrial applications is becoming increasingly significant.[10–12] Various synthesis routes for TMD nanomaterials exist, broadly categorized into top-down methods like mechanical cleavage, liquid or chemical exfoliation, and bottom-up approaches, such as chemical vapor deposition, hydrothermal and colloidal syntheses.[13–15] The colloidal method is particularly attractive for its ability to address the limitations of exfoliation methods, such as low yield, and the high costs associated with chemical vapor deposition.[16–20] Typically, colloidal synthesis of TMD catalysts involves the use of organic solvents/ligands, such as oleylamine or formamide.[21,22] However, with the goal of scaling up the synthesis for future industrial use, cheaper and more environmentally friendly solvents have to be employed, especially taking into account the fact that the contribution of organic solvents used in large quantities to the whole process costs is very often dominant. Here, water would be an ideal solution, as the most abundant and cheapest solvent, thus offering safety, environmental sustainability, and cost-effectiveness. A key advancement in aqueous synthesis was made by Ding et al., who successfully synthesized defective small TMD nanoparticles.[23] The defects may enhance the activity of reactive oxygen species, although it is important to consider that long-chain organic ligands present on these nanoparticles might impede their catalytic efficiency. Additionally, the complexity of pH regulation in the aqueous synthesis of nanoparticles and their relatively low yield remain challenges for widespread industrial application. Thus, developing aqueous synthesis methods that maintain the high catalytic performance of TMD nanoparticles is a crucial goal.

The European Union's goal to produce 20 million tons of green hydrogen by 2030 underscores the importance of sustainable energy practices.[24] Proton exchange membrane (PEM) electrolyzer cells play a critical role in this endeavor, emerging as an efficient means to generate high-purity hydrogen from renewable sources. The main challenge in PEM electrolysis, particularly for the HER, lies in creating efficient, affordable, and stable cathode electrocatalysts that do not depend on noble metals.[25,26] TMD nanoparticles, with their exceptional catalytic properties and cost-effectiveness, are a promising solution. Integrating TMD nanoparticles into PEM electrolyzer cells could markedly improve the efficiency and sustainability of hydrogen production, representing a potential paradigm shift in the field and leading the way to more eco-friendly and economically feasible hydrogen production technologies.

In this study, we present a novel aqueous synthesis method for TMD nanoparticles, including MoS_2, $MoSe_2$, RuS_2, and $RuSe_2$. This synthesis is carried out under mild conditions, successfully circumventing the need for organic solvents/ligands, high temperatures, pressures, or specialized equipment. Among the synthesized TMD nanomaterials, $RuSe_2$ nanoparticles achieve an impressively low overpotential of just 37 mV to reach current densities of 10 mA cm^{-2}, along with a Tafel slope of 48 mV dec^{-1} in 0.5 M H_2SO_4. Remarkably, these $RuSe_2$ nanoparticles also demonstrate superior HER performance in alkaline and phosphate-buffered saline (PBS) solutions, rivaling that of commercial Pt/C electrodes. Additionally, in practical PEM water electrolysis applications, $RuSe_2$ nanoparticles also show outstanding cell performance. At current densities of 1 A cm^{-2}, the required cell voltages are only 2.07 V. We believe this research paves the way to economical and sustainable synthesis methods, with significant potential for industrial-scale HER applications.

2. Results and Discussion

2.1. Synthesis and Characterization of Various TMD Nanoparticles

The synthesis of TMD nanoparticles developed here involves a bottom-up, aqueous method conducted at room temperature, utilizing a simple chemical reaction between chalcogen (S or Se) and metal (Mo or Ru) precursors. **Figure 1** provides a schematic overview of the synthesis procedure, while detailed descriptions can be found in the experimental section. The process starts with the dissolution of the chalcogen precursor in water. Unlike the straightforward preparation of the Na_2S solution, the selenium precursor is formed by the reaction of elemental selenium with an insufficient amount of the reducing agent, sodium borohydride ($NaHB_4$), leading to the formation of corresponding diselenide.[27] In an aqueous medium, $MoCl_5$ quickly hydrolyses, generating hydrochloric acid, shifting pH to the lower values, and inducing protonation of sulfides and selenides.[28] Protonated sulfides can participate in redox reactions with metal ions giving corresponding dithiol and diselenide species according to Equations (1) and (2).[29] In the case of sodium sulfide, we may assume that some amount of disulfide can be generated by an alternative path. The process of dissolution of Na_2S in water can generate hydroxyl anions and facilitate the solubilization of molecular oxygen, as shown in Equation (3).[30] This environment sets the stage for the sulfide autooxidation reaction, where sulfur ions react with oxygen and hydroxyl ions to form disulfide ions along with electron release. Finally, the metal cations (Mo^{4+} or Ru^{3+}) react with dithiols or diselenides giving corresponding TMD nanoparticles, as shown in Equation (4).[30]

$$M_{aq}^{x+} + 2HS^- \rightarrow M_{aq}^{(x-1)+} + 2HS\bullet \quad (1)$$

$$2HS\bullet \rightarrow HSSH \quad (2)$$

$$2S^{2-} \xrightarrow{O_2 + OH^-} S_2^{2-} \quad (3)$$

$$M_{aq}^{x-1} + \left[X_2^{2-}\right] \rightarrow MX_2 \quad (4)$$

The experiment deliberately uses high concentrations of precursors to synthesize small-sized TMD nanoparticles. High precursor concentration often leads to the formation of numerous nuclei in colloidal synthesis. Taking the synthesis of MoS_2 as an example, during the reaction, the Mo-precursor in high concentration exhibited an orange color (Figure S1a, Supporting Information), while the resulting product particles displayed a brownish color with a large amount of precipitates (Figure S1b, Supporting Information). The resulting TMD nanomaterials are synthesized without any ligands, facilitating easy upscaling and making them suitable for direct application as electrocatalysts without

© 2024 The Author(s). Advanced Functional Materials published by Wiley-VCH GmbH

16163028, 0, Downloaded from https://onlinelibrary.wiley.com/doi/10.1002/adfm.202404565 by Readcube (Labtiva Inc.), Wiley Online Library on [04/06/2024]. See the Terms and Conditions (https://onlinelibrary.wiley.com/terms-and-conditions) on Wiley Online Library for rules of use; OA articles are governed by the applicable Creative Commons License

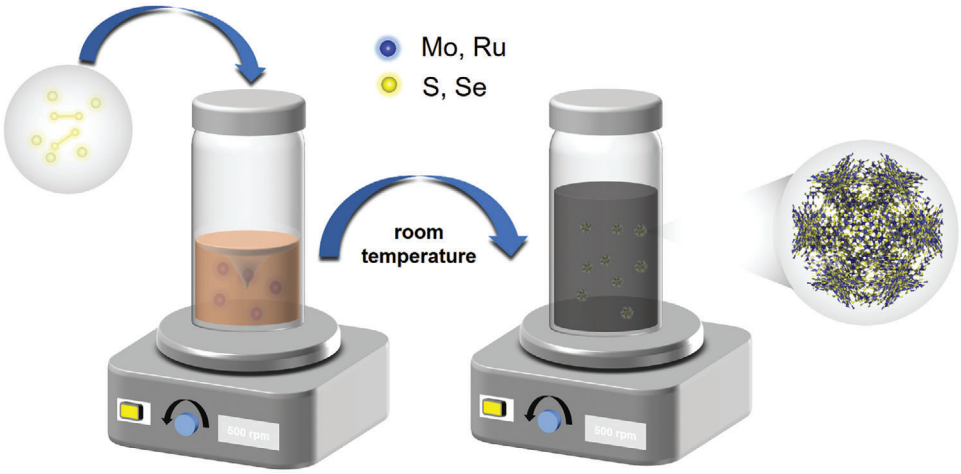

Figure 1. Schematic illustration of the synthesis of TMD nanoparticles.

any additional treatment, such as high-temperature annealing or ligand exchange. By conducting the reaction at room temperature for less than 1 min, we obtained nanoparticles at a yield of above 95%, underscoring the efficiency and speed of our synthesis method. The overall method presents a novel approach to synthesizing TMD nanoparticles, offering a significant advancement in material science due to its simplicity, efficiency, and adaptability to various conditions.

The morphology of TMD nanomaterials was investigated by transmission electron microscopy (TEM) imaging. As shown in **Figure 2a–d**, TEM images reveal that these materials exhibit an irregular morphology and tendency to agglomeration. This agglomeration is caused by the absence of ligands and the diminutive size of the particles. We further performed high-resolution TEM (HRTEM) imaging on the MoS_2 and $RuSe_2$ samples to analyze their structure and morphology, as displayed in Figure 2e,f. This characterization revealed that MoS_2 nanoparticles crystallize in the trigonal prismatic 2H phase with distinct lattice spacings of 0.623 nm corresponding to the (002) crystal faces of the MoS_2 structure. In contrast, HRTEM images of $RuSe_2$ show lattice spacings of 0.590, 0.290, and 0.265 nm, which correspond to the (001), (002), and (210) crystal faces of the cubic $RuSe_2$ structure. In order to estimate the size of MoS_2 nanoparticle aggregates in water dispersions, from which they were processed into thin films, we conducted dynamic light scattering (DLS) measurements. These measurements disclosed a bimodal size distribution of the aggregates (as depicted in Figure S2, Supporting Information), with an average size of ≈200 nm. The particles in water exhibited an average zeta potential of −26.4 mV (refer to Figure S3, Supporting Information), which accounts for their colloidal stability.

We further characterized the structure and composition of the TMD nanoparticles using Raman spectroscopy, powder X-ray diffraction (XRD) analysis, and X-ray photoemission spectroscopy (XPS). The Raman spectrum depicted in **Figure 3a** highlights distinct peaks at 377 cm^{-1} (E^1_{2g} mode) and 402 cm^{-1} (A_{1g} mode) for MoS_2 nanoparticles. These peaks are directly linked to in-plane and out-of-plane vibrations, respectively, serving as definitive indicators of the 2D nanostructure of MoS_2 nanoparticles.[31,32] Additionally, few-monolayer thick MoS_2 nanoflakes show a preferential orientation along the [002] direction indicated by the disappearance of certain peaks in their XRD pattern displayed in Figure 3b (XRD patterns of other materials are shown in Figure S4, Supporting Information). XPS measurements were utilized to analyze the composition and oxidation states of both Mo and S in the MoS_2 nanoparticles. Figure 3c,d present the high-resolution core-level XPS spectra of S 2p and Mo 3d, respectively. The S 2p signal can be deconvoluted into two sets of doublets. The main doublet observed at binding energies of 162.5 and 163.6 eV aligns with divalent sulfide ions, assigned to the basal plane S^{2-} species inherent to MoS_2. The second doublet appearing at 163.8 and 164.9 eV can be assigned to disulfide S_2^{2-} species located along the edge of MoS_2, which is widely recognized as an unsaturated sulfur edge.[33] The appearance of an S—O feature we attribute to unavoidable surface oxidation. The Mo 3d spectrum consists of a single doublet at 229.9 and 233.1 eV, corresponding to the $3d_{5/2}$ and $3d_{3/2}$ orbitals of Mo^{4+} in MoS_2, respectively.[34] The Raman spectrum and high-resolution core-level XPS spectra of Se 3d, Ru 3p, and Ru 3d of $RuSe_2$ nanoparticles, which showed the best catalytic performance, were also thoroughly analyzed (Figure S5, Supporting Information). Due to the low crystallinity of the $RuSe_2$ nanoparticles, only one peak at 235 cm^{-1} was clearly detected, while the peak at 165 cm^{-1} remained indistinct, as illustrated in Figure S5a (Supporting Information).[35] Figure S5b (Supporting Information) presents the Se 3d core-level signal, featuring two distinct peak regions at 55.4 and 54.5 eV, corresponding to Se $3d_{3/2}$ and Se $3d_{5/2}$, respectively, which are associated with the Ru—Se bond. Additionally, peaks at 59.0 and 58.2 eV arise from SeO_x, indicative of surface oxidation under ambient conditions.[36] Ru 3d and Ru 3p peaks, displayed in Figure S5c,d (Supporting Information), further confirm the formation of $RuSe_2$.

2.2. Electrochemical Performance

The electrochemical performance of various TMD nanomaterials was investigated in a three-electrode cell within a wide pH range. In this study, we employed the drop-casting method to deposit the catalysts on the surfaces of the working electrodes. All the

© 2024 The Author(s). Advanced Functional Materials published by Wiley-VCH GmbH

16163028, 0, Downloaded from https://onlinelibrary.wiley.com/doi/10.1002/adfm.202404565 by Readcube (Labtiva Inc.), Wiley Online Library on [04/06/2024]. See the Terms and Conditions (https://onlinelibrary.wiley.com/terms-and-conditions) on Wiley Online Library for rules of use; OA articles are governed by the applicable Creative Commons License

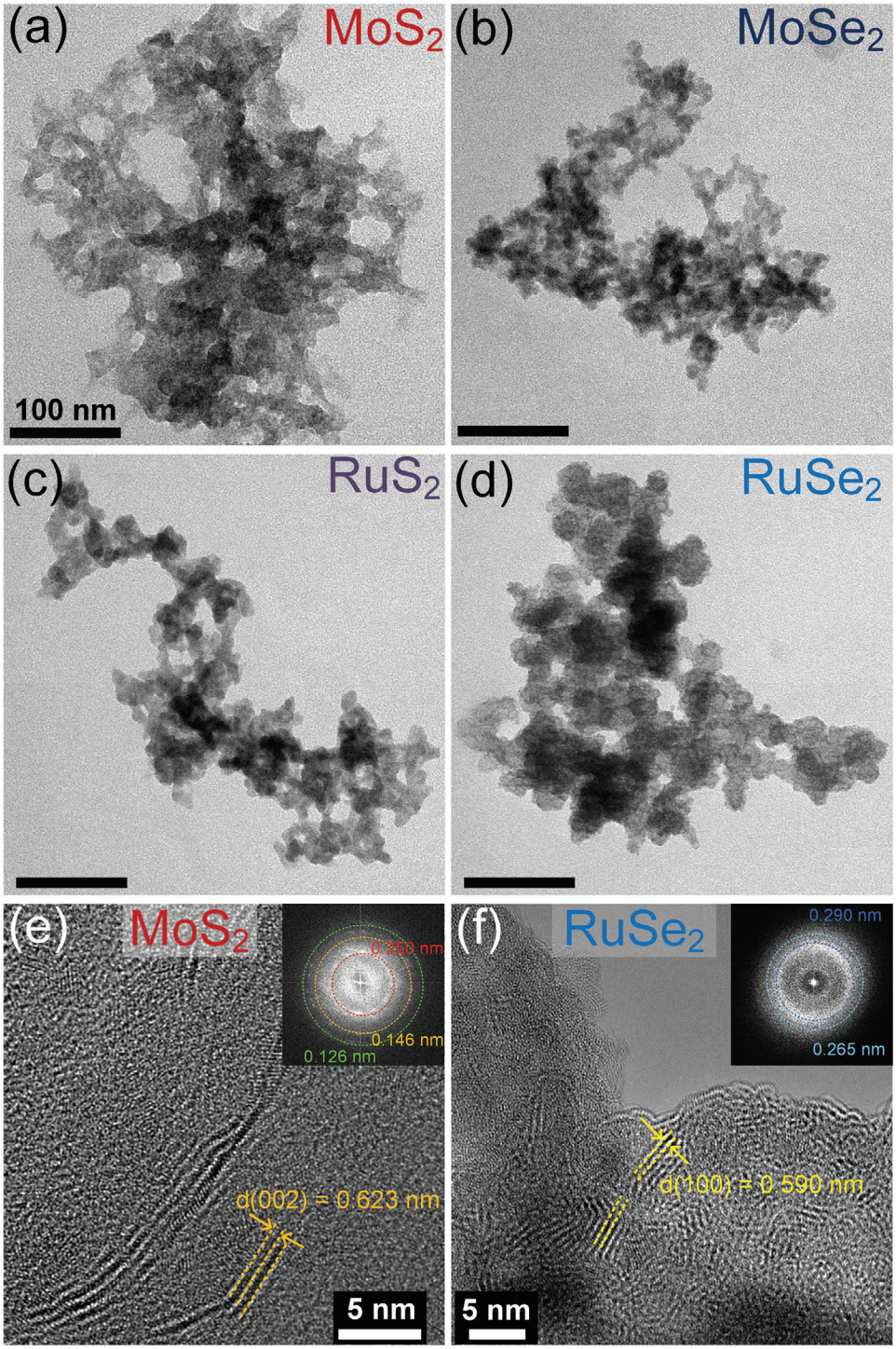

Figure 2. Conventional TEM images of MoS_2 a), $MoSe_2$ b), RuS_2 c), and $RuSe_2$ d) nanoparticles. All scale bars are 100 nm. HRTEM images of $MoSe_2$ e) and $RuSe_2$ f) nanoparticles with corresponding FFT (fast Fourier transform) patterns revealing distinct lattice spaces with 0.623, 0.250, 0.146, and 0.126 nm in MoS_2 e), as well as 0.590, 0.290, and 0.265 nm in $RuSe_2$ f).

 © 2024 The Author(s). Advanced Functional Materials published by Wiley-VCH GmbH

16163028, 0, Downloaded from https://onlinelibrary.wiley.com/doi/10.1002/adfm.202404565 by Readcube (Labtiva Inc.), Wiley Online Library on [04/06/2024]. See the Terms and Conditions (https://onlinelibrary.wiley.com/terms-and-conditions) on Wiley Online Library for rules of use; OA articles are governed by the applicable Creative Commons License

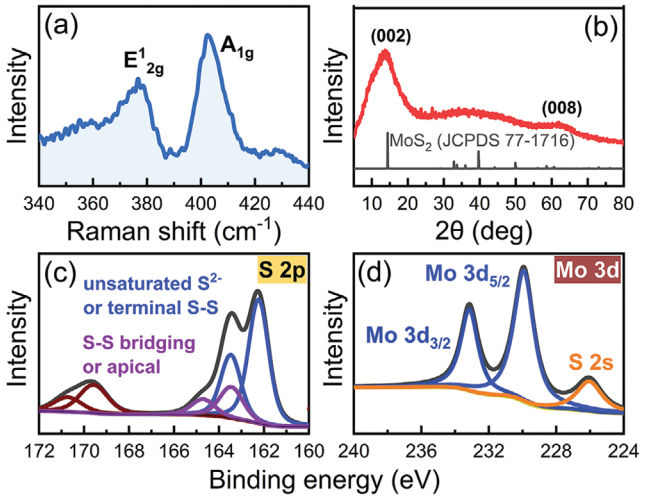

Figure 3. Raman spectrum a), XRD pattern (with corresponding bulk reference of 2H MoS_2 (JCPDS 77–1716)) b), high-resolution XPS core-level signals of S 2p c) and Mo 3d d) of MoS_2 nanoparticles.

electrochemical tests were performed without IR compensation. We initially evaluated the electrocatalytic HER behavior of TMD nanoparticles in an acidic media (0.5 M H_2SO_4, pH 0), comparing their performance with commercial Pt/C catalysts under the same conditions. **Figure** 4a displays the linear sweep voltammetry (LSV) curves of different nanomaterials, among which $RuSe_2$ nanoparticles showed outstanding catalytic performance, which surpassed MoS_2, $MoSe_2$, and RuS_2 nanoparticles, and even was comparable to the commercial Pt/C. Notably, at the current density of 10 mA cm^{-2}, $RuSe_2$ nanoparticles required only 37 mV which is highly competitive with Pt/C (28 mV). In contrast, the corresponding values for MoS_2, $MoSe_2$, and $RuSe_2$ nanoparticles were 70, 112, and 161 mV, respectively. Figure 4b summarizes the Tafel slopes of these nanomaterials, which indicate the reaction kinetics of the catalytic process. As seen in the plot, apart from Pt/C (34 mV dec^{-1}), $RuSe_2$ nanoparticles achieve the smallest Tafel slope value of 48 mV dec^{-1}, indicating superior charge transfer efficiency and faster reaction kinetics compared to MoS_2 (72 mV dec^{-1}), $MoSe_2$ (85 mV dec^{-1}), and RuS_2 (66 mV dec^{-1}) nanoparticles. The histogram in Figure 4c visualizes the performance metrics, specifically overpotential at 10 mA cm^{-2} and Tafel slope values of different TMD nanomaterials, demonstrating the favorable electrocatalytic activity of $RuSe_2$ nanoparticles in an acidic medium.

To get further insights into interfacial reactions and electron transfer kinetics under HER conditions we employed electrochemical impedance spectroscopy (EIS). As depicted in Figure 4d, the charge transfer resistance of $RuSe_2$ nanoparticles was registered at 12.39 Ω, showcasing superior performance compared to MoS_2 (60 Ω), $MoSe_2$ (95.4 Ω), and RuS_2 (27.15 Ω). This pronounced difference underscores the favorable electron transport and catalytic kinetics exhibited by $RuSe_2$, emphasizing its potential as a promising material for HER applications. The double-layer capacitance (C_{dl}) values were derived by analyzing the non-Faradaic capacitive currents from cyclic voltammetry scans conducted at various scan rates (Figure S6, Supporting Information). This method facilitated the determination of

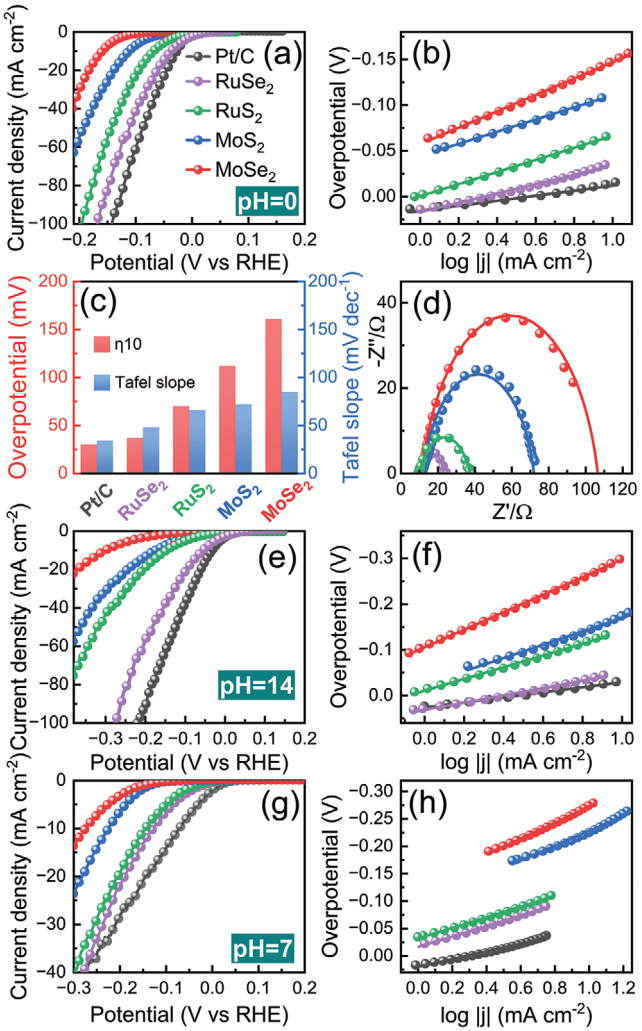

Figure 4. HER performance of different TMD nanoparticles ($RuSe_2$, RuS_2, MoS_2, and $MoSe_2$) in different media varying from strongly acidic to strongly alkaline. LSV curves a), Tafel plots b), comparison of the Tafel slope values at the current density of 10 mA cm^{-2} c), and Nyquist plots of electrochemical impedance spectra of the nanoparticles in 0.5 M H_2SO_4 solution (pH 0). LSV curves e) and Tafel plots f) in 1 M KOH solution (pH 14). LSV curves g) and Tafel plots h) in 1 M PBS (pH 7).

the electrochemical surface area (ECSA) and, subsequently, the intrinsic activity of the materials. The MoS_2 nanoparticles show the highest C_{dl} of 15.05 mF cm^{-2}, as compared to $RuSe_2$ (8.59 mF cm^{-2}), RuS_2 (3.68 mF cm^{-2}), and $MoSe_2$ (1.74 mF cm^{-2}) nanoparticles, as depicted in Figure S7 (Supporting Information). It should be pointed out that the C_{dl} value of $RuSe_2$ is not the largest. Consequently, the superior HER catalytic performance of $RuSe_2$ sample is attributed to its elevated intrinsic activity rather than a larger ECSA. Taken together, these results suggest that an optimal balance between a large ECSA and a high intrinsic activity is crucial for achieving exceptional electrocatalytic performance.[37] To eliminate the influence of mass loading and to better understand the intrinsic catalytic activity, the mass activity was determined by normalizing the observed current density to the catalyst amount. The loading mass of various TMD

© 2024 The Author(s). Advanced Functional Materials published by Wiley-VCH GmbH

16163028, 0, Downloaded from https://onlinelibrary.wiley.com/doi/10.1002/adfm.202404565 by Readcube (Labtiva Inc.), Wiley Online Library on [04/06/2024]. See the Terms and Conditions (https://onlinelibrary.wiley.com/terms-and-conditions) on Wiley Online Library for rules of use; OA articles are governed by the applicable Creative Commons License

particles is summarized in Table S1 (Supporting Information). As demonstrated in Figure S8 (Supporting Information), the $RuSe_2$ catalyst exceeds 250 mA mg^{-1} in an acidic medium at an overpotential of 100 mV, which is the highest value among the TMD nanoparticles. We further calculated the turnover frequency (TOF) for all catalysts. This approach aims to provide a more accurate assessment of the intrinsic activity. The hydrogen TOF values calculated from the ECSA and the polarization curves are plotted in Figure S9 (Supporting Information). $RuSe_2$ sample displays a TOF of 0.45 H_2 s^{-1} and 1.47 H_2 s^{-1} at 100 and 200 mV overpotential, respectively, which are the highest values among these catalysts. In conclusion, $RuSe_2$ nanoparticles synthesized at room temperature are small and exhibit low crystallinity, which results in a significant number of defects on the basal surface. Consequently, this leads to a marked increase in the exposure of active edge sites which is beneficial to the HER performance.

An electrocatalyst capable of withstanding localized pH variations on its surface plays a crucial role in safeguarding the electrode against corrosion during extended periods of electrolysis. Such a pH-universal catalyst, possessing high activity for the HER, holds immense appeal for a range of operating conditions. Therefore, the HER performance of the samples was also examined in an alkaline medium (1 M KOH, pH 14) and neutral medium (1 M PBS, pH 7). As can be observed from the LSV curves in Figure 4e, $RuSe_2$ nanoparticles showed better HER performance, requiring only 53 mV to achieve the current density of 10 mA cm^{-2} compared to MoS_2 (145 mV), $MoSe_2$ (191 mV), and RuS_2 (128 mV) nanoparticles. In the alkaline medium, except for Pt/C, $RuSe_2$ nanoparticles also demonstrated a smaller Tafel slope value of 79 mV dec^{-1} compared to MoS_2 (145 mV dec^{-1}), $MoSe_2$ (191 mV dec^{-1}), and RuS_2 (128 mV dec^{-1}) nanoparticles shown in Figure 4f. In the neutral PBS, except for Pt/C catalyst, the best catalytic material was still $RuSe_2$ nanoparticles, which only required a low overpotential of 129 mV to achieve a current density of 10 mA cm^{-2} (Figure 4g), along with a Tafel slope of 95 mV dec^{-1} (Figure 4h). In this study, we compared the C_{dl} and TOF values of $RuSe_2$ nanoparticles in various media, as shown in Figure S10 (Supporting Information). Our findings reveal that $RuSe_2$ exhibits superior catalytic performance in acidic conditions. This better activity in acidic medium is attributed to the fact that HER in alkaline solutions experiences relatively slower kinetics compared to acidic environments, thereby necessitating higher overpotentials to drive the reaction.[38] Thus, $RuSe_2$ nanoparticles synthesized exhibited HER performance comparable to and in many cases surpassing that of other colloidal TMDs already published to date, as summarized in Table S2 (Supporting Information). All the characterizations performed and discussed above indicate that the TMD nanoparticles synthesized at room temperature using a very simple approach can act as a highly active electrocatalyst for HER in a wide pH range. It is worth noting that $RuSe_2$ nanoparticles demonstrate catalytic performance closely comparable to that of the commercial Pt/C catalyst (taking into account that Ru has the 1/3 price of Pt metal).

We further analyzed the changes in the composition of MoS_2 and $RuSe_2$ catalysts after subjecting them to 2000 cycles of cyclic voltammetry testing in 0.5 M H_2SO_4. The XPS core-level signals of Ru 3d and Se 3d showed no noticeable change in the chemical states of both elements, indicating generally good stability of the material (Figure S11, Supporting Information). We note that the shift toward higher binding energies observed in SeO_x is likely a consequence of inter-site electron transfer and a redistribution of charge on the surface.[39] In contrast, there is no obvious shift in the binding energies of the high-resolution S 2p and Mo 2p spectra of MoS_2. Notably, we observed an increase in the concentration of the higher valence S_2^{2-} component, suggesting that S^{2-} is prone to be reduced, leading to the formation of S_2^{2-}. Additionally, the emergence of the doublet corresponding to Mo^{6+} can be attributed to similar electron transfer processes. These results suggest that the $RuSe_2$ nanoparticles demonstrate exceptional electrocatalytic activity and durability for the HER, indicating their potential as a pH-universal electrocatalyst for this application.

To demonstrate the scalability of our aqueous synthesis of TMD nanoparticles, we expanded the reaction volume by a factor of 100 (Figures S12 and S13, Supporting Information). The catalytic performance of the upscaled MoS_2 and $RuSe_2$ nanoparticles, as shown in Figure S14 (Supporting Information), was consistent with that observed in the smaller batch samples. This finding strongly indicates that our synthesis method for these TMD nanomaterials is not only effective but also readily scalable to at least gram-scale production, without any compromise in their superior HER performance. Further, we tested upscaled MoS_2 and $RuSe_2$ nanoparticles as cathode materials in a PEM electrolyzers for HER. We evaluated catalytic properties of both $RuSe_2$ and MoS_2 nanoparticles in the PEM electrolyzer featuring a 5 cm^2 active area. The electrolyzer operated under a dry-cathode configuration, with only the anode compartment being continuously supplied with hot (80 °C) MilliQ water at a flow rate of 40 mL per minute. In contrast, the cathode compartment remained dry and was exposed to the atmosphere, as depicted in **Figure 5a**. To establish a benchmark, we prepared a membrane electrode assembly (MEA) containing commercial Pt-black, a well-known reference catalyst for HER. Recognizing that various experimental parameters can affect the MEA's performance, complicating direct comparison with existing literature, our study focused on comparing the performance of MEAs containing $RuSe_2$ or MoS_2 with that of the Pt-black reference MEA. Figure 5b displays the polarization curves of MEAs with $RuSe_2$ and MoS_2 nanoparticles, as well as Pt-black as cathode catalysts in the PEM electrolyzer. Notably, the MEA with $RuSe_2$-based cathode catalyst exhibited superior performance compared to the MoS_2 nanoparticle catalysts which is consistent with results obtained on the three-electrode cell system discussed above. In our electrolysis setup, we achieved a significant current density of 1 A cm^{-2} at applied potentials of 2.07 V for $RuSe_2$ nanoparticles, 2.28 V for MoS_2 nanoparticles, and 1.90 V for the Pt-black cathode catalysts, respectively.

Initially, the impact of combining $RuSe_2$ or MoS_2 with an electrically conductive material (carbon black) on the performance of PEM electrolysis was examined. In this context, a physical mixture of the catalytic material with carbon black at different weight ratios (1:0, 3:1, 1:1, and 1:3) was assessed as a cathode catalyst, maintaining a constant catalyst amount (2 mg cm^{-2}) while varying the carbon black quantity. In the electrolyzer setup, IrO_2 was utilized as the anode catalyst. The electrical conductivity of the catalyst is an important factor in designing electrodes. Adding electrically conductive materials, such as carbon black, to the active catalyst could be beneficial for charge transport and distribution. At the same time, if the amount of the additive is too large,

© 2024 The Author(s). Advanced Functional Materials published by Wiley-VCH GmbH

16163028, 0, Downloaded from https://onlinelibrary.wiley.com/doi/10.1002/adfm.202404565 by Readcube (Labtiva Inc.), Wiley Online Library on [04/06/2024]. See the Terms and Conditions (https://onlinelibrary.wiley.com/terms-and-conditions) on Wiley Online Library for rules of use; OA articles are governed by the applicable Creative Commons License

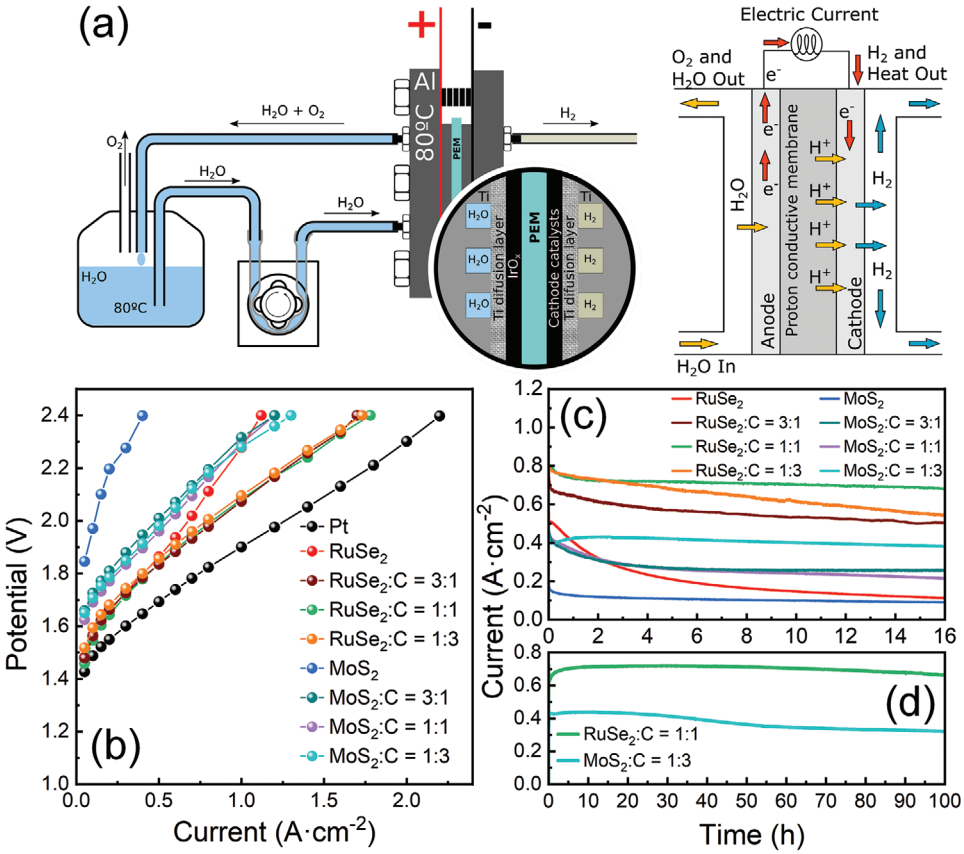

Figure 5. A principal scheme of the electrolyzer in a dry-cathode configuration a). Polarization curves performed galvanostatically for MEAs containing $RuSe_2$ or MoS_2 pure or mixed with carbon black at different weight ratios: nanoparticles:carbon = 3:1, 1:1, and 1:3, compared with the performance of commercial Pt-black catalyst b). Stability tests of MEAs containing $RuSe_2$ or MoS_2 pure or mixed with carbon black at different ratios over 16 h c) and two catalyst compositions $ReSe_2$:C = 1:1 and MoS_2:C = 1:3 over 100 h d) of continuous operation at 2 V.

it could negatively affect catalytic activities by blocking a fraction of the active catalytic sites.[40,41] Within the current range of 0.05–0.5 A cm^{-2}, no significant differences were observed among the various ratios of $RuSe_2$ and carbon black. However, at higher currents, bare $RuSe_2$ exhibited lower performance compared to the mixture of nanoparticles with carbon black. At higher current densities, the MEA containing the 1:1 ratio of $RuSe_2$ to carbon black showed the best performance. In contrast, for the MoS_2 catalyst, the performance of the MEA was significantly lower without carbon black, emphasizing the substantial impact of the additive in enhancing the catalyst's conductivity. In the case of MoS_2, at lower current densities, the MEA with a 1:1 ratio of catalyst:carbon black had a higher performance. However, at higher currents, the performance pattern shifted, with better results observed on the MEA containing a 1:3 ratio of catalyst:carbon black.

To evaluate the stability of the catalysts we conducted chronoamperometric tests on various MEAs prepared (Figure 5c). Chronoamperometric measurements were carried out at 2.0 V for 16 h, maintaining a water flow rate of 40 mL min^{-1} and a working temperature of 80 °C. The results of the stability tests reveal that MEAs prepared without carbon black exhibited lower currents. Specifically, MEAs containing bare $RuSe_2$ nanoparticles demonstrated poor stability over time. Conversely, the addition of carbon black to the catalyst significantly enhanced the current. In the case of $RuSe_2$, MEAs with $RuSe_2$ to carbon black ratios of 3:1 and 1:1 exhibited the best stability. A constant current of 0.71 A cm^{-2} sustained for at least 16 h was achieved with the MEA containing a 1:1 mixture of $RuSe_2$:carbon black. However, higher amounts of the additive led to decreased stability, as an excessive carbon black can obstruct active sites, thereby reducing MEA performance. For the MoS_2 catalyst, optimal performance was achieved with a nanoparticles:carbon black ratio of 1:3. This mixture yielded a stable current of 0.41 A cm^{-2} for a minimum of 16 h. The best performing and the most stable compositions $ReSe_2$:C = 1:1 and MoS_2:C = 1:3 were further tested over a longer timescale of 100 h, results are displayed in Figure 5d. While $ReSe_2$:C = 1:1 catalyst maintained its excellent performance, the performance of MoS_2:C = 1:3 composite slightly decreased after ≈30 h. Such outstanding long-term catalytic stability promises that our nanoparticles can serve as high-efficiency HER electrocatalysts for large-scale practical applications.

3. Conclusion

We have developed an aqueous synthesis approach for preparing a range of TMD nanomaterials, including MoS_2, RuS_2, $MoSe_2$, and $RuSe_2$, under mild conditions. This process enables the

© 2024 The Author(s). Advanced Functional Materials published by Wiley-VCH GmbH

16163028, 0, Downloaded from https://onlinelibrary.wiley.com/doi/10.1002/adfm.202404565 by Readcube (Labtiva Inc.), Wiley Online Library on [04/06/2024]. See the Terms and Conditions (https://onlinelibrary.wiley.com/terms-and-conditions) on Wiley Online Library for rules of use; OA articles are governed by the applicable Creative Commons License

production of TMD nanoparticles on at least a gram-scale, without compromising their excellent catalytic performance in the HER. Notably, our synthesis method is both environmentally friendly and economical. In a three-electrode system, $RuSe_2$ nanoparticles stand out among various TMD compounds for their exceptional HER performance. These nanoparticles demonstrate capabilities that rival those of the benchmark Pt/C electrode across a broad pH range. Specifically, at a current density of 10 mA cm^{-2}, the $RuSe_2$ nanoparticles require only a minimal overpotential of 37 mV in 0.5 M H_2SO_4, 53 mV in 1 M KOH, and 95 mV in 1 M PBS. Crucially, in a PEM water electrolyzer, MoS_2 and $RuSe_2$ nanoparticles achieved impressive current densities of 1 A cm^{-2} at cell voltages of 2.28 and 2.07 V, respectively, and a longtime stability over 100 h. As cathode catalysts, they present a viable alternative to platinum-group metals in PEM water electrolysis. This breakthrough positions our synthesis method as highly promising for the large-scale production of electrocatalysts and their further industrial application.

4. Experimental Section

Chemicals: Sodium sulfide (Na_2S, ≤100%), molybdenum chloride ($MoCl_5$, 95%), selenium (Se, 99.999%), sodium borohydride ($NaHB_4$, 95%), sulfuric acid (95%), and ruthenium(III)-chloride hydrate ($RuCl_3 \times H_2O$, 99%) were purchased from Acros Organics; carbon black (Vulcan XC-72R) and Aquivion E98-15S membrane were purchased from Fuel Cell Store; ethanol (anhydrous, >99%) and potassium hydroxide (KOH, 90%) were purchased from Merck. IrO_2 (>99%, powder) and platinum black (high surface area of 25.0–30.4 m^2 g^{-1}) were purchased from Alfa Aesar; Nafion solution (Nafion™ perfluorinated resin solution, 20 wt.% in lower aliphatic alcohols and water), potassium phosphate monobasic (KH_2PO_4, 99%), and potassium phosphate dibasic (K_2HPO_4, 99%) were purchased from Sigma Aldrich.

Synthesis of MoS_2 Nanoparticles: 27.3 mg (0.1 mmol) of $MoCl_5$ were dissolved in 1 mL of ultrapure water, whereupon hydrogen chloride was generated and the color of the solution quickly turned light orange, followed by bubbling with nitrogen for 10 min to remove air. In parallel, 157 mg (2 mmol) of Na_2S were dissolved in 10 mL of ultrapure water and bubbled with nitrogen for 5 min. Then, 1 mL of thus prepared S-precursor solution was injected into the Mo-precursor solution upon vigorous stirring at room temperature. The color of the mixture quickly changed from orange to black, the product nanoparticles precipitated when stirring was stopped after 2 min. The resulting MoS_2 nanoparticles were purified by adding 1 mL of ethanol, followed by centrifugation at 5200 rpm for 30 s, and cleaned with water twice. The precipitate was dispersed in 4 mL of ethanol.

Synthesis of Other TMD Nanoparticles: The protocol was similar to that for MoS_2 nanoparticles. The only difference was the preparation of a Se-precursor. In a typical procedure, 79.9 mg of Se powder was added to 5 mL of $NaBH_4$ (60 mg) aqueous solution to reduce it at ambient conditions. After 30 min reaction, black Se powder was completely dissolved forming a red solution. For the synthesis of $RuSe_2$, RuS_2, and $MoSe_2$ nanoparticles, similar quantities and the same mild conditions were employed, as described in the MoS_2 nanoparticle synthesis above.

The synthesis of MoS_2 (the cheapest material) and $RuSe_2$ (best-performing material) nanoparticles was upscaled. For the preparation of MoS_2 nanoparticles, 2.73 g of $MoCl_5$ were dissolved in 100 mL of MilliQ water in a 500 mL bottle accompanied by a release of HCl forming white smoke, then bubbled 30 min with nitrogen. In parallel, 1.57 g of Na_2S were dissolved in 100 mL of pure water in a 100 mL bottle. Thus prepared S-precursor was poured into the Mo-precursor bottle upon vigorous stirring, forming a precipitate. The resulting MoS_2 nanoparticles were purified by adding 100 mL of ethanol followed by centrifugation. For the synthesis of $RuSe_2$ nanoparticles, 2.07 g of $RuCl_3$ were dissolved in 100 mL of MilliQ water in a 500 mL bottle, followed by bubbling with nitrogen for 30 min. To prepare the Se-precursor, 0.8 g of Se powder were added to 100 mL of $NaBH_4$ (0.6 g) aqueous solution to reduce it at ambient conditions upon stirring at 500 rpm. When the color changed into transparent red, the Se-precursor was quickly added to the Ru-precursor bottle upon vigorous stirring. The resulting $RuSe_2$ nanoparticles were purified similarly to MoS_2 ones.

Transmission Electron Microscopy (TEM): Bright-field TEM imaging on a Zeiss Libra 120 transmission electron microscope operated at 120 kV was used to characterize the morphology of the nanomaterials. For TEM specimen preparation, the corresponding nanoparticles were purified three times with water and then drop-cast from diluted water dispersions onto carbon-coated copper grids. *High resolution TEM (HRTEM) imaging* was conducted on a Thermo Fisher Spectra 300 STEM equipped with double aberration correction, operating at 200 kV. The sample was diluted with ethanol and then dropped onto lacey carbon grids for subsequent image acquisition.

Raman Spectroscopy: Raman spectra of the nanomaterials were acquired on a high-resolution confocal Raman microscope MonoVista CRD+ (S&I Spectroscopy & Imaging GmbH) with a liquid-nitrogen cooled CCD PyLoN: 100 BRX detector (Princeton Instruments). The samples were prepared by drop-casting nanoparticles from ethanol on a microscope slide followed by drying in air. The spectra were recorded with 514 nm laser excitation and a power of ≈0.6 mW on the sample.

X-Ray Diffraction (XRD) Analysis: Powder XRD patterns were collected in the reflection mode with a Bruker AXS D2 PHASER instrument equipped with a nickel filter and a LYNXEYE/SSD160 detector, using Cu $K\alpha_{1,2}$ irradiation.

X-Ray Photoemission Spectroscopy (XPS): First, ethanol was evaporated from nanoparticle dispersions by bubbling with nitrogen. Then, the resulting powders were deposited on a Kapton tape and transferred to an ultrahigh vacuum chamber (ESCALAB 250Xi by Thermo Scientific, base pressure 2×10^{-10} mbar) for the XPS measurements. To evaluate the samples before and after the electrochemical test, we measured them directly onto a carbon cloth, which was used as a working electrode (see below). The measurements were carried out using an XR6 monochromatized Al $K\alpha$ source ($h\nu$ = 1486.6 eV) and a pass energy of 20 eV. An additional flood gun was used in order to prevent charging. The binding energy scale was internally referenced to the C 1s peak at 285 eV.

The size distribution and zeta potential of MoS_2 nanoparticles in water were characterized by a *dynamic light scattering (DLS)* system Malvern Zetasizer Nano ZSP.

Electrochemical Tests: A three-electrode measurement setup was used to carry out the measurements. The setup consists of a reference electrode (Ag/AgCl in a saturated KCl in 0.5 M H_2SO_4 or 1 M PBS; Hg/HgO electrode in 1 M KOH), a counter electrode (graphite rods), and a glassy carbon disk working electrode with a diameter of 3 mm (geometric area of 0.07 cm^2). A sample kept in 4 mL of ethanol was first sonicated for homogenization, and then 0.5 mL of this dispersion was centrifuged. The precipitate together with 1 mg of carbon black was dispersed in 1 mL of an isopropanol/water mixture (1/3-vol.) and sonicated for 1 h followed by stirring for 1 h. Subsequently, the thus obtained dispersion was drop-cast on the surface of the glassy carbon electrode and dried in air. This deposition was repeated three times to form a thicker layer of the nanomaterials, amounting to ≈0.229 mg cm^{-2}. To evaluate the stability of nanoparticles following the HER test, the same amount of materials was uniformly deposited onto a carbon cloth. Electrochemical impedance spectroscopy measurements were performed in the frequency range from 0.1 Hz to 10 000 kHz at 140 mV versus RHE. Cyclic voltammetry characterization was carried out at 100–200 mV versus RHE. TOF can be defined as $TOF = \frac{J\,N_A}{2Fn\ (ESCA)}$, here J is the current density at a given overpotential, N_A is Avogadro's number (6.023×10^{23}), F is the Faraday constant (96 485.4 C mol^{-1}), the factor two is the number of electrons required to form one hydrogen molecule, and n is the number of active sites per cm^2.

Proton Exchange Membrane Electrolyzer Assembly and Testing: First, inks for the membrane fabrication were prepared. The inks comprised a

© 2024 The Author(s). Advanced Functional Materials published by Wiley-VCH GmbH

16163028, 0, Downloaded from https://onlinelibrary.wiley.com/doi/10.1002/adfm.202404565 by Readcube (Labtiva Inc.), Wiley Online Library on [04/06/2024]. See the Terms and Conditions (https://onlinelibrary.wiley.com/terms-and-conditions) on Wiley Online Library for rules of use; OA articles are governed by the applicable Creative Commons License

mixture that included IrO_2 for the anode, and either synthesized $RuSe_2$ or MoS_2, along with carbon black (Vulcan XC 72) for the cathode, MilliQ water, isopropanol, and Nafion solution. The mixture was prepared in the following weight ratio: 1 part catalyst and carbon black mixture, 100 parts water, 200 parts isopropanol, to 0.85 parts Nafion solution. The inks underwent two consecutive rounds of sonication using a Bandelin Sonopuls HD 4200 Ultrasonic Homogenizers for 30 s each, in an ice bath.

Membrane electrode assembly (MEA) was fabricated as follows: The Aquivion E98-15S membrane (150 µm thick, Fuel Cell Store) was used as the polymer electrolyte membrane which was treated before use. The treatment process involved washing the membrane successively in a 5% H_2O_2 solution for 1 h at 80 °C, followed by immersion in a 0.5 M sulfuric acid solution for 1 h at 80 °C and concluding with cleaning using MilliQ water for 1 h at 100 °C. These treated membranes were subsequently stored in water at room temperature until use. The prepared ink formulations were deposited onto the pretreated membrane (5 cm^2 active area and a total membrane area of 16 cm^2). The inks were sprayed through a custom-made automatic spray system, with a consistent catalyst loading of 2 mg cm^{-2} of IrO_2 for the anode and 2 mg cm^{-2} of either $RuSe_2$, MoS_2, or Pt for the cathode.

The deposition process was carried out by spraying inks on the membrane attached to a vacuum table heated to 90 °C. The resulting MEA was then subjected to hot-pressing using a manual hot press for 2 min at 120 °C at ≈1700 N cm^{-2}. In all experiments, the loading of catalysts ($RuSe_2$ or MoS_2) was kept constant at 2 mg cm^{-2}, while the amount of carbon black was varied.

Electrolysis tests were conducted with a commercial electrolyzer cell obtained from the Fuel Cell Store (photos of the setup are displayed in Figures S15–S17, Supporting Information). The prepared MEA was inserted into the cell, positioned between two 5 cm^2 Ti porous gas diffusion layers, and then sandwiched between two Ti current collector plates. This assembly, including the metallic housing of the electrolyzer, was closed using PTFE gaskets and with the help of aluminum end plates, applying a torque of 5 Nm. Electrical insulation for the end plates was maintained using silicon gaskets. For water supply, MilliQ water was consistently delivered at a rate of 40 mL min^{-1} and maintained at 80 °C to the anode side through a peristaltic pump. The working temperature of 80 °C was controlled using a temperature control system integrated with the aluminum end plates, which were equipped with heating accessories. To apply the desired potential or current, a Keysight E36731A battery emulator was employed. Polarization curves were taken galvanostatically with 5 min step durations. A cut-off cell voltage at 2.4 V was used during the experiments. To determine the catalyst stability, chronoamperometry experiments at 2.0 V for 16 h and 100 h were carried out. The evolved gases (O_2 and H_2) were released into the atmosphere through the outlets.

Supporting Information

Supporting Information is available from the Wiley Online Library or from the author.

Acknowledgements

The authors thank Markus Göbel (TU Dresden) for Raman measurements. J.L. acknowledges the China Scholarship Council (No. 202006750019). Y.V. has received funding from the European Research Council (ERC) under the European Union's Horizon 2020 research and innovation program (ERC grant agreement 714067, ENERGYMAPS). This work was partially financed by the Catalan Government through the funding grant ACCIÓ-Eurecat (Project TRAÇA – GreenH_2). ICN2 acknowledges funding from Generalitat de Catalunya 2021SGR00457. This study is part of the Advanced Materials programme and was supported by MCIN with funding from European Union NextGenerationEU (PRTR-C17.I1) and by Generalitat de Catalunya. J.Y. and J.A. thank the support from the project NANOGEN (PID2020-116093RB-C43), funded by MCIN/ AEI/10.13039/501100011033/ and by "ERDF A way of making Europe", by the "European Union". ICN2 is supported by the Severo Ochoa program from Spanish MCIN / AEI (Grant No.: CEX2021-001214-S) and is funded by the CERCA Programme / Generalitat de Catalunya. Part of the present work has been performed in the framework of the Universitat Autònoma de Barcelona Materials Science PhD program. J.Y. has received funding from the CSC-UAB PhD scholarship program. The authors acknowledge the use of instrumentation as well as the technical advice provided by the Joint Electron Microscopy Center at ALBA (JEMCA). ICN2 acknowledges funding from Grant IU16-014206 (METCAM-FIB) provided by the European Union through the European Regional Development Fund (ERDF), with the support of the Ministry of Research and Universities, Generalitat de Catalunya. ICN2 is a founding member of e-DREAM.[42]

Open access funding enabled and organized by Projekt DEAL.

Conflict of Interest

The authors declare no conflict of interest.

Data Availability Statement

The data that support the findings of this study are available from the corresponding author upon reasonable request.

Keywords

aqueous synthesis, efficient hydrogen generation, facile upscale, proton exchange membrane water electrolyzer, transition metal dichalcogenide nanoparticles

Received: March 15, 2024
Revised: May 10, 2024
Published online:

[1] X. Dai, K. Du, Z. Li, M. Liu, Y. Ma, H. Sun, X. Zhang, Y. Yang, *ACS Appl. Mater. Interfaces* **2015**, *7*, 27242.
[2] N. K. Shrestha, S. A. Patil, A. S. Salunke, A. I. Inamdar, H. Im, *J. Mater. Chem. A* **2023**, *11*, 14870.
[3] H. S. Chavan, C. H. Lee, A. I. Inamdar, J. Han, S. Park, S. Cho, N. K. Shreshta, S. U. Lee, B. Hou, H. Im, H. Kim, *ACS Catal.* **2022**, *12*, 3821.
[4] H. Wang, L. Gao, *Curr. Opin. Electrochem.* **2018**, *7*, 7.
[5] D. Voiry, J. Yang, M. Chhowalla, *Adv. Mater.* **2016**, *28*, 6197.
[6] Z. Chen, K. Leng, X. Zhao, S. Malkhandi, W. Tang, B. Tian, L. Dong, L. Zheng, M. Lin, B. S. Yeo, K. P. Loh, *Nat. Commun.* **2017**, *8*, 14548.
[7] M.-R. Gao, M. K. Y. Chan, Y. Sun, *Nat. Commun.* **2015**, *6*, 7493.
[8] D. Voiry, M. Salehi, R. Silva, T. Fujita, M. Chen, T. Asefa, V. B. Shenoy, G. Eda, M. Chhowalla, *Nano Lett.* **2013**, *13*, 6222.
[9] C. Xu, S. Peng, C. Tan, H. Ang, H. Tan, H. Zhang, Q. Yan, *J. Mater. Chem. A* **2014**, *2*, 5597.
[10] Z.-Y. Zhao, F.-L. Li, Q. Shao, X. Huang, J.-P. Lang, *Adv. Mater. Interfaces* **2019**, *6*, 1900372.
[11] J.-Y. Xue, F.-L. Li, Z.-Y. Zhao, C. Li, C.-Y. Ni, H.-W. Gu, D. J. Young, J.-P. Lang, *Inorg. Chem.* **2019**, *58*, 11202.
[12] W.-Z. Chen, M. Zhang, Y. Liu, X.-M. Yao, P.-Y. Liu, Z. Liu, J. He, Y.-Q. Wang, *Appl. Catal. B Environ.* **2024**, *340*, 123145.
[13] B. Zhao, D. Shen, Z. Zhang, P. Lu, M. Hossain, J. Li, B. Li, X. Duan, *Adv. Funct. Mater.* **2021**, *31*, 2105132.
[14] H. Li, J. Wu, Z. Yin, H. Zhang, *Acc. Chem. Res.* **2014**, *47*, 1067.
[15] R. Lv, J. A. Robinson, R. E. Schaak, D. Sun, Y. Sun, T. E. Mallouk, M. Terrones, *Acc. Chem. Res.* **2015**, *48*, 56.
[16] C. Meerbach, B. Klemmed, D. Spittel, C. Bauer, Y. J. Park, R. Hübner, H. Y. Jeong, D. Erb, H. S. Shin, V. Lesnyak, A. Eychmüller, *ACS Appl. Mater. Interfaces* **2020**, *12*, 13148.

© 2024 The Author(s). Advanced Functional Materials published by Wiley-VCH GmbH

16163028, 0, Downloaded from https://onlinelibrary.wiley.com/doi/10.1002/adfm.202404565 by Readcube (Labtiva Inc.), Wiley Online Library on [04/06/2024]. See the Terms and Conditions (https://onlinelibrary.wiley.com/terms-and-conditions) on Wiley Online Library for rules of use; OA articles are governed by the applicable Creative Commons License

[17] C. Backes, T. M. Higgins, A. Kelly, C. Boland, A. Harvey, D. Hanlon, J. N. Coleman, *Chem. Mater.* **2017**, *29*, 243.
[18] M. Nasilowski, B. Mahler, E. Lhuillier, S. Ithurria, B. Dubertret, *Chem. Rev.* **2016**, *116*, 10934.
[19] I. Song, C. Park, H. C. Choi, *RSC Adv.* **2014**, *5*, 7495.
[20] J. H. Han, S. Lee, J. Cheon, *Chem. Soc. Rev.* **2013**, *42*, 2581.
[21] Z. Liu, K. Nie, X. Qu, X. Li, B. Li, Y. Yuan, S. Chong, P. Liu, Y. Li, Z. Yin, W. Huang, *J. Am. Chem. Soc.* **2022**, *144*, 4863.
[22] J. Li, R. Hübner, M. Deconinck, A. Bora, M. Göbel, D. Schwarz, G. Chen, G. Wang, S. A. Yang, Y. Vaynzof, V. Lesnyak, *ACS Appl. Nano Mater.* **2023**, *6*, 9475.
[23] X. Ding, F. Peng, J. Zhou, W. Gong, G. Slaven, K. P. Loh, C. T. Lim, D. T. Leong, *Nat. Commun.* **2019**, *10*, 41.
[24] A. Piñeiro García, D. Perivoliotis, X. Wu, E. Gracia-Espino, *ACS Sustainable Chem. Eng.* **2023**, *11*, 7641.
[25] A. Kumar Samuel, A. H. Faqeeh, W. Li, Z. Ertekin, Y. Wang, J. Zhang, N. Gadegaard, D. A. J. Moran, M. D. Symes, A. Y. Ganin, *ACS Sustainable Chem. Eng.* **2024**, *12*, 1276.
[26] A. Morozan, H. Johnson, C. Roiron, G. Genay, D. Aldakov, A. Ghedjatti, C. T. Nguyen, P. D. Tran, S. Kinge, V. Artero, *ACS Catal.* **2020**, *10*, 14336.
[27] A. Capperucci, A. Petrucci, D. Tanini, *Arkivoc* **2023**, 202211959.
[28] S. Dolci, F. Marchetti, G. Pampaloni, S. Zacchini, *Dalton Trans.* **2010**, *39*, 5367.
[29] C. F. Cullis, J. D. Hopton, C. J. Swan, D. L. Trimm, *J. Appl. Chem.* **1968**, *18*, 335.
[30] D. Díaz, S. E. Castillo-Blum, O. Álvarez-Fregoso, G. Rodríguez-Gattorno, P. Santiago-Jacinto, L. Rendon, L. Ortiz-Frade, Y.-J. León-Paredes, *J. Phys. Chem. B* **2005**, *109*, 22715.
[31] M. A. Pimenta, E. del Corro, B. R. Carvalho, C. Fantini, L. M. Malard, *Acc. Chem. Res.* **2015**, *48*, 41.
[32] H. Li, Q. Zhang, C. C. R. Yap, B. K. Tay, T. H. T. Edwin, A. Olivier, D. Baillargeat, *Adv. Funct. Mater.* **2012**, *22*, 1385.
[33] Y. Dong, Z. Zhu, Y. Hu, G. He, Y. Sun, Q. Cheng, I. P. Parkin, H. Jiang, *Nano Res.* **2021**, *14*, 74.
[34] N. P. Kondekar, M. G. Boebinger, E. V. Woods, M. T. McDowell, *ACS Appl. Mater. Interfaces* **2017**, *9*, 32394.
[35] W. Zhan, N. Li, S. Zuo, Z. Guo, C. Qiang, Z. Li, J. Ma, *CrystEngComm* **2022**, *24*, 620.
[36] Z. Zhang, C. Jiang, P. Li, K. Yao, Z. Zhao, J. Fan, H. Li, H. Wang, *Small* **2021**, *17*, 2007333.
[37] H.-J. Liu, S. Zhang, Y.-M. Chai, B. Dong, *Angew. Chem.* **2023**, *135*, 202313845.
[38] J. Wei, M. Zhou, A. Long, Y. Xue, H. Liao, C. Wei, Z. J. Xu, *Nano-Micro Lett.* **2018**, *10*, 75.
[39] J. Hu, C. Zhang, P. Yang, J. Xiao, T. Deng, Z. Liu, B. Huang, M. K. H. Leung, S. Yang, *Adv. Funct. Mater.* **2020**, *30*, 1908520.
[40] J. Ampurdanés, M. Chourashiya, A. Urakawa, *Catal. Today* **2019**, *336*, 161.
[41] T. Corrales-Sánchez, J. Ampurdanés, A. Urakawa, *Int. J. Hydrogen Energy* **2014**, *39*, 20837.
[42] M. Botifoll, I. Pinto-Huguet, J. Arbiol, *Nanoscale Horiz.* **2022**, *7*, 1427.

© 2024 The Author(s). Advanced Functional Materials published by Wiley-VCH GmbH

16163028, 0, Downloaded from https://onlinelibrary.wiley.com/doi/10.1002/adfm.202404565 by Readcube (Labtiva Inc.), Wiley Online Library on [04/06/2024]. See the Terms and Conditions (https://onlinelibrary.wiley.com/terms-and-conditions) on Wiley Online Library for rules of use; OA articles are governed by the applicable Creative Commons License